Contents lists available at ScienceDirect

European Journal of Mechanics / B Fluids

Turbulence in the rotating-disk boundary layer investigated through direct numerical simulations

E. Appelquist [a,b], P. Schlatter [a,b], P.H. Alfredsson [a,*], R.J. Lingwood [a,c]

[a] Linné FLOW Centre, KTH Mechanics, Royal Institute of Technology, S-100 44 Stockholm, Sweden
[b] Swedish e-Science Research Centre (SeRC), SE-100 44 Stockholm, Sweden
[c] Division of Engineering Science, School of Engineering and Materials Science, Queen Mary University of London, Mile End Road, London E1 4NS, UK

ARTICLE INFO

ABSTRACT

Direct numerical simulations (DNS) are reported for the turbulent rotating-disk boundary layer for the first time. Two turbulent simulations are presented with overlapping small and large Reynolds numbers, where the largest corresponds to a momentum-loss Reynolds number of almost 2000. Simulation data are compared with experimental data from the same flow case reported by Imayama et al. (2014), and also a comparison is made with a numerical simulation of a two-dimensional turbulent boundary layer (2DTBL) over a flat plate reported by Schlatter and Örlü (2010). The agreement of the turbulent statistics between experiments and simulations is in general very good, as well as the findings of a missing wake region and a lower shape factor compared to the 2DTBL. The simulations also show rms-levels in the inner region similar to the 2DTBL. The simulations validate Imayama et al.'s results showing that the rotating-disk turbulent boundary layer in the near-wall region contains shorter streamwise (azimuthal) wavelengths than the 2DTBL, probably due to the outward inclination of the low-speed streaks. Moreover, all velocity components are available from the simulations, and hence the local flow angle, Reynolds stresses and all terms in the turbulent kinetic energy equation are also discussed. However there are in general no large differences compared to the 2DTBL, hence the three-dimensional effects seem to have only a small influence on the turbulence.

1. Introduction

This paper investigates the turbulent rotating-disk boundary layer, which arises over a disk rotating in otherwise quiescent fluid. In contrast to a flat-plate boundary layer, the boundary layer on the rotating disk is three-dimensional. The flow is dragged along with the rotating disk, but it also has a radial outward component, the so-called crossflow component, and to fulfil mass conservation, fluid is drawn towards the disk from the non-rotating fluid outside the boundary layer. If the boundary layer is laminar, a similarity solution exists as shown in 1921 by von Kármán [1]. For the laminar rotating-disk flow, a convenient measure of the Reynolds number is the nondimensional radius, defined as

$$R = r^* \sqrt{\frac{\Omega^*}{\nu}} = r, \qquad (1)$$

where $*$ refers to a dimensional quantity, r^* is the radial position on the disk and $\delta^* = \sqrt{\nu/\Omega^*}$ is the length scale used, where ν

is the (dimensional) kinematic viscosity of the fluid and Ω^* is the angular velocity of the disk.

The laminar rotating-disk boundary layer experiences a primary global instability at a Reynolds number that depends on the azimuthal wavenumber β and below which the flow field always starts to transition to turbulence; e.g. for $\beta = 68$ Appelquist et al. [2] found $R = 583$. In experiments, a secondary global instability due to the presence of stationary cross-flow vortices triggers the transition process for even lower Reynolds numbers, $R = 510$–520 [3,4]. As an example, a disk with a radius of 25 cm rotating at 1400 revolutions per minute in air will experience start of transition at a radial distance of about 16 cm from the centre of the disk and a boundary layer that becomes fully turbulent a few more centimetres further radially outwards, hence the boundary layer leaving the disk will be turbulent. For a recent review of previous and current research on the stability properties of the rotating-disk flow see [5].

The laminar boundary layer existing at lower R has a constant boundary-layer thickness that does not vary in the radial direction. This feature changes when the flow becomes turbulent, the thickness increases over the transition region and continues to increase with r^* as the boundary layer becomes fully turbulent.

Table 1
Summary of the spectral-element mesh for the smaller turbulent simulation (R1) in terms of size of the domain [min max], number of spectral elements (N_r, N_θ and N_z in the r, θ and z directions, respectively) and the resolution of the spectral elements in the radial, azimuthal and wall-normal directions in the equidistant region. The total number of spectral elements is 259,067. Additionally information on the time is also given where T is the total time in rotations, N_T the number of timesteps and ΔT the length of the timestep.

$r = [200\ 650]$	$N_r = 137$	$\Delta r = 3$
$\theta = [0\ 2\pi/12]$	$N_\theta = 61$	$\Delta\theta = 2\pi/(12 \times N_\theta)$
$z = [0\ 49]$	$N_z = 31$	$\Delta z = 0.4, s = 1.08$
$T = [0\ 4.625]$	$N_T = 3.33 \times 10^6$	$\Delta T = 1.39 \times 10^{-6}$

Several experiments of this turbulent boundary layer have already been carried out [6–10] and also one large-eddy-simulation study has been reported [11]. In all these experiments one of the major difficulties arises from the thinness of the boundary layer, which makes even single hot-wire measurements hard to carry out close to the wall and more or less excludes multi-wire probes to be used, at least close to the wall. Hence, experimental turbulence data are scarce for this flow, and those that have been reported also suffer from spatial resolution issues.

There are at least two major differences compared to the two-dimensional turbulent boundary layer, namely the three-dimensionality of the flow and the inflow towards the disk from the undisturbed region above the disk. However the experiments show that the crossflow component is rather weak, the flow angle at the wall was found to be 11° by Refs. [6,9]. In the experiments by Littell and Eaton [8], X-probes were used and both the radial and azimuthal mean velocity components were obtained and they showed a similar angle at their closest points to the disk (at a wall distance of approximately 100 viscous units). The near-wall region has been experimentally examined by Refs. [9] and [10] and Imayama et al. [10] found a lower turbulence intensity of the azimuthal velocity component in the near-wall region compared with the streamwise fluctuation level in a two-dimensional turbulent boundary layer over a flat plate (2DTBL). Differences were also found in the outer region in line with previous results (e.g. Refs. [8,11]), such as a missing (or weak) wake region.

In the present work, DNS results for the turbulent rotating-disk boundary layer are presented. The advantage of the DNS as compared to experiments is that there is no interference between measurement equipment and the wall, and it is possible to obtain all velocity components including the turbulent stresses and other correlations. The results are compared, where possible, with the results from Ref. [10], but also with a 2DTBL simulation [12]. The new simulations are described in Section 2 and results are presented and discussed in Section 3. Finally a summary is given in Section 4.

2. Simulations

2.1. Simulation code Nek5000

The simulations were performed with the massively parallel code Nek5000 [13] using a Spectral Element Method (SEM). The code solves the full incompressible Navier–Stokes equations

$$\frac{\partial \mathbf{U_x}}{\partial t} + \mathbf{U_x} \cdot \nabla \mathbf{U_x} = -\nabla p + \frac{1}{Re_s} \nabla^2 \mathbf{U_x} + \mathbf{f_x} \tag{2}$$

together with the continuity equation

$$\nabla \cdot \mathbf{U_x} = 0, \tag{3}$$

where $\mathbf{U_x} = (u_x, u_y, w)$ are the velocities in Cartesian coordinates, p is the pressure, Re_s is the simulation Reynolds number and $\mathbf{f_x}$ is a forcing term used in connection with the initial tripping, fictional forces (if included) and a sponge region are sometimes used

Table 2
Turbulent simulation R2, for captions see Table 1. The total number of spectral elements is 932,170.

$r = [400\ 800]$	$N_r = 194$	$\Delta r = 2$
$\theta = [0\ 2\pi/13.6]$	$N_\theta = 155$	$\Delta\theta = 2\pi/(13.6 \times N_\theta)$
$z = [0\ 49]$	$N_z = 31$	$\Delta z = 0.4, s = 1.08$
$T = [0\ 4.125]$	$N_T = 2.97 \times 10^6$	$\Delta T = 1.39 \times 10^{-6}$
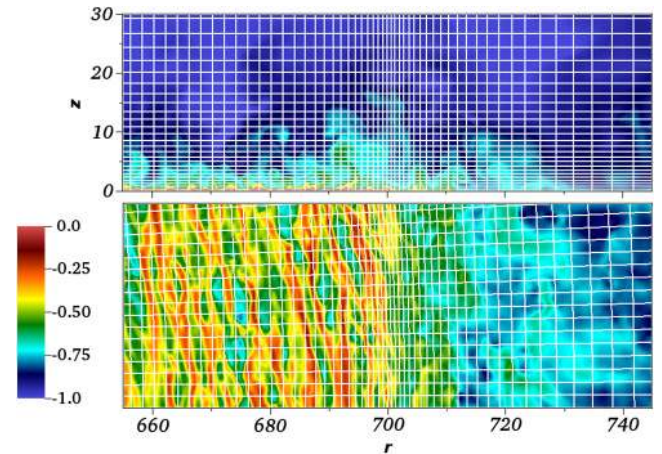
Fig. 1. Illustration of the distribution of the spectral elements for case R2. Slices for $T = 1.75$ shown in the rotating reference frame at (a) $\theta = 0$ and (b) $z = 0.4$ ($z^+ \approx 12.5$ for these $R < 700$). The colour shows the azimuthal velocity in the rotating frame of reference, i.e. the velocity is zero at the disk surface and -1 far away. At $R > 700$ one observes the damping of the turbulence when the flow leaves the disk. (For interpretation of the references to colour in this figure legend, the reader is referred to the web version of this article.)

together with the radial boundary conditions. For the velocities in cylindrical coordinates, $\mathbf{U} = (u, v, w)$ are used corresponding to the radial (r), azimuthal (θ) and wall-normal (z) directions. The time-scale within Nek5000 is such that t corresponds to the number of radians through which the disk has rotated. The number of full rotations is measured by $T = t/(2\pi)$. For further reading on the solver and use of the code the reader is referred to [13–16].

2.2. Computational mesh

Two simulations were made named R1 and R2, and their spectral-element meshes are given in Tables 1 and 2 together with temporal information. All lengths are normalized with δ^* and time with the time period for one revolution. Within each element, a spectral mesh is used with the polynomial order 7. The radial ranges are different for each of the two simulations, R1 focuses on small radial positions (low Reynolds numbers) and R2 focuses on large r. For both simulations, the elements are equidistant up to either $r = 542$ or 682 and then clustered towards the disk edge at either $r = 560$ or $r = 700$, respectively. This is illustrated together with an instantaneous field for case R2 in Fig. 1 however only a part of the spectral-element mesh is shown.

In the wall-normal direction the elements are stretched according to

$$z_n = \frac{s^n - 1}{s - 1} \Delta z, \tag{4}$$

where s is the stretching factor, z_n is the coordinate at position n above the wall and $z_1 = \Delta z$ is the height of the spectral element closest to the wall. The values of these and other parameters are shown in Tables 1 and 2.

In wall-bounded turbulent flows the resolution of the mesh needs to be evaluated based on the inner (viscous) length scale

$\ell_*^* = \nu/v_\tau^*$. Here, v_τ^* is the azimuthal friction velocity defined by the azimuthal wall shear stress $\tau_{w,\theta}^*$,

$$v_\tau^* = \sqrt{\frac{\tau_{w,\theta}^*}{\rho}} = \sqrt{\frac{\mu}{\rho}\left|\frac{\partial V^*}{\partial z^*}\right|_{z=0}} = \sqrt{\nu\left|\frac{\partial V^*}{\partial z^*}\right|_{z=0}} \qquad (5)$$

where V^* is the mean azimuthal velocity (in the following capital letters (U, V, W) denote mean velocities, and (u', v', w') denote the corresponding fluctuations around the mean), ρ and μ are the dimensional density and dynamic viscosity, respectively. Note that u_τ^* can be defined similarly by using the wall shear stress in the radial direction. The friction velocity (v_τ^*) is used to nondimensionalize the azimuthal velocity and rms to become $V^+ = V^*/v_\tau^*$ and $v_{rms}^+ = v_{rms}^*/v_\tau^*$ (similarly for $U^+ = U^*/v_\tau^*$ and $u_{rms}^+ = u_{rms}^*/v_\tau^*$), and the viscous length scale normalize the wall-normal distance $z^+ = z^*/\ell_*^*$.

However, since all velocities presented herein are normalized using the local azimuthal wall velocity $V_w^* = \Omega^* r^*$ and the normalizing length scale is $\delta^* = \sqrt{\nu/\Omega^*}$ it may be more illuminating to express the friction velocity and the viscous length scale normalized with these quantities, which gives:

$$\frac{v_\tau^*}{V_w^*} = v_\tau = (\Delta_w/r)^{1/2} \quad \text{and} \quad \frac{\ell_*^*}{\delta^*} = \ell_* = (\Delta_w r)^{-1/2}, \qquad (6)$$

where Δ_w is the nondimensional wall gradient

$$\Delta_w = \frac{\delta^*}{V_w^*}\left|\frac{\partial V^*}{\partial z^*}\right|_{z=0}. \qquad (7)$$

Although, due to our already nondimensionalized simulations the actual calculation of v_τ involves an artificial viscosity ($\nu_s = Re_s^{-1}$, see Eq. (2)), giving

$$v_\tau = \sqrt{\nu_s\left|\frac{\partial V}{\partial z}\right|_{z=0}} \quad \text{and} \quad \ell_* = \frac{\nu_s}{v_\tau}.$$

In our case ν_s is set to one.

The spatial resolution of the mesh can be expressed in inner scale units in all directions, Δz^+, Δr^+ and $r\Delta\theta^+$ shown in Fig. 2 for both simulation cases. The resolution varies across the spectral elements due to the spectral mesh. In (a) and (b), Δz^+ is shown as a function of radius and height. The first point in each mesh is below $z^+ = 0.8$ (0.35) for all radial positions and there are at least five (eleven) points below $z^+ = 10$. The values in parentheses correspond to the best resolved local values. The contour of $\Delta z^+ = 10$ is shown in black. In (c) and (d), Δr^+ is shown with the average resolution in red. In (e) and (f), only the minimum and maximum resolutions across a spectral element in terms of $r\Delta\theta^+$ are shown as a function of radius. It is clear that the resolution is higher for smaller r and z due to the cylindrical formation of the elements. The time step in the simulation corresponds to less than approximately 0.01 viscous time unit.

2.3. Boundary and initial conditions

The boundary conditions were the same as used by [2] and are briefly described below. The flow velocities at the disk were specified as no-slip and non-penetration conditions, and for the top boundary condition the following combination of Dirichlet and stress-free conditions was used: the perturbation velocities in the wall-parallel directions were set to zero ($u_x = 0$ and $u_y = 0$), whereas the wall-normal velocity (w) was set to follow the stress-free Neumann boundary condition for the corresponding weak formulation. Outwards of the disk edge, located at $r = 560$ (R1) or 700 (R2), the surface was assigned a symmetric boundary condition. For this condition the domain is mirrored in the z-direction and the physical geometry of the simulation then corresponds

to an infinitely-thin disk where $W = 0$, and $\partial U/\partial z = 0$ and $\partial V/\partial z = 0$. Farther outwards, prior to the outer radial boundary specified by the stress-free Neumann boundary condition, there was a weak sponge that force the azimuthal velocity component to zero and the wall-normal component to a weak updraft. The segmentation of the domain from the full rotating annulus to a section was made possible through cyclic boundary conditions in the azimuthal direction, which are essentially periodic boundary conditions but involve an appropriate rotation of the velocities across the boundary.

Both simulations started with the von Kármán similarity solution over the full domain. Initially, an undisturbed laminar flow was simulated such that the flow could adapt to the symmetry boundary condition radially outwards from the disk edge. At $T = 1/8$, a trip forcing was turned on and the turbulent flow started evolving.

2.4. Turbulence trip

The trip forcing used is described in detail in Ref. [17], it is here transferred to the rotating-disk geometry. The tripping is a weak, random volume force acting in the wall-normal direction and can be thought of as a strip of velcro tape commonly used in experiments to trip the incoming flow over e.g. a flat plate. In the present case the trip strip is added along a line in the azimuthal direction at a radial position of 230 for the low Reynolds number simulation (R1) and at 430 for the high Reynolds number simulation (R2). The number of modes used were 11 and 25 in the azimuthal direction, respectively. The reason for the higher mode number for case R2 is due to the longer strip line for a larger radial position. The extent in the radial direction is determined by a Gaussian distribution, with a standard deviation given by $4\delta_{1,95}$, where $\delta_{1,95} = 1.2$ is the displacement thickness of the von Kármán laminar boundary layer (see Eq. (8) below). The extent of the trip forcing in the wall-normal direction is also determined by a Gaussian function with a standard deviation of $\delta_{1,95}$, where the centre location is at $z = 0$, i.e. only using half the function. The trip in our simulations has a time-dependent amplitude that fluctuates over a time scale $t_s = 2\pi/180$. The magnitude of the disturbance is ten times larger for R1 than for R2.

2.5. Data handling

During the course of the simulations several instantaneous fields were saved. Additionally, various quantities were temporally averaged every 10th timestep to get enough data for statistical calculations, e.g. mean velocities and higher moments. Since the mean value was not known during the simulations the velocities and their higher moments were themselves averaged whereafter the different moments could be calculated. For instance, if $u_i = \overline{U_i} + u_i'$ then the mean $\overline{U_i}$, and the variance, skewness and flatness of u_i' can be evaluated from averages of u_i, u_i^2, u_i^3 and u_i^4. Also, more complex quantities like transport terms in the turbulent kinetic energy equation or the dissipation can be evaluated in a similar manner. This is further elaborated in Appendix.

3. Results

In this section the results from the simulations are presented both in terms of integral flow parameters as function of radial distance and distributions of the mean velocities, flow angles and higher moments as function of the distance from the disk surface at seven different Reynolds numbers, namely $r = 261, 328, 397, 464, 530, 601, 669$. In Section 3.1 the integral quantities of the flow are defined and shown how they vary with

(a) R1, Δz^+.

(b) R2, Δz^+.

(c) R1.

(d) R2.

(e) R1.

(f) R2.
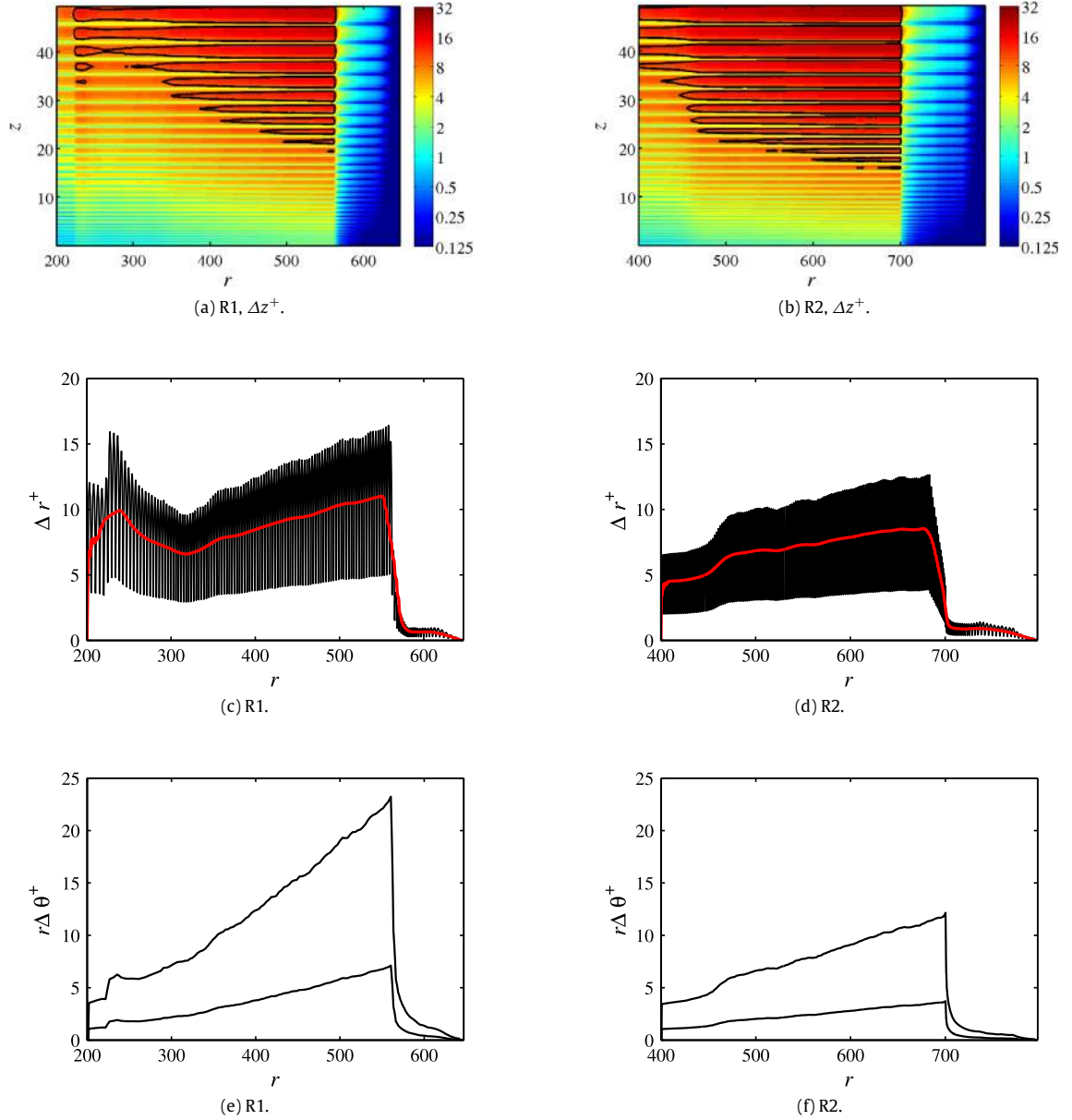
Fig. 2. Resolution of the two meshes in plus units. The Δz^+ colours in (a) and (b) are shown in $\log_2$ scale, and contour of $\Delta z^+ = 10$ is shown in black. In (c) and (d) the average resolution of Δr^+ is shown in red. In (e) and (f) only minimum and maximum resolutions of $r\Delta\theta^+$ are shown. (For interpretation of the references to colour in this figure legend, the reader is referred to the web version of this article.)

Reynolds number for the two different simulations R1 and R2 and in Section 3.2 the mean flow is shown. In Section 3.3 the variances (rms), skewness and all three Reynolds shear stress terms are shown as well as the turbulent kinetic energy budget. Also, the Townsend structure parameter, A_1, which gives an indication of the strength of the three-dimensionality is investigated and compared with the 2DTBL. Instantaneous velocity field are shown in Section 3.4, whereas Section 3.5 gives spectral information of the turbulence. Where possible the results are compared with the experiments at the two Reynolds number by Imayama et al. [10], denoted in their paper as T01 and T02, at $r = 668$ and 698, respectively. The corresponding momentum-loss thickness Reynolds numbers, R_θ, are 1704 and 1926. In [10] the experimental results were also compared with 2DTBL simulation results by Schlatter and Örlü [12] at low but similar Reynolds numbers. Here, we chose to do the comparison with the two-dimensional case for $R_\theta = 1420$, denoted by 2D01 in [10].

3.1. Integral flow quantities

The azimuthal velocity can be normalized with the wall velocity in the laboratory frame to become $V_N(z) = V(z)/V(0) = V(z)/V_W$. Two boundary-layer thicknesses, δ_{95} and δ_{99}, can also be defined as the distances from the disk where $V_N = 0.05$ and $V_N = 0.01$, respectively. Based on these heights, the displacement thicknesses $\delta_{1,95}$ and $\delta_{1,99}$ can also be defined as
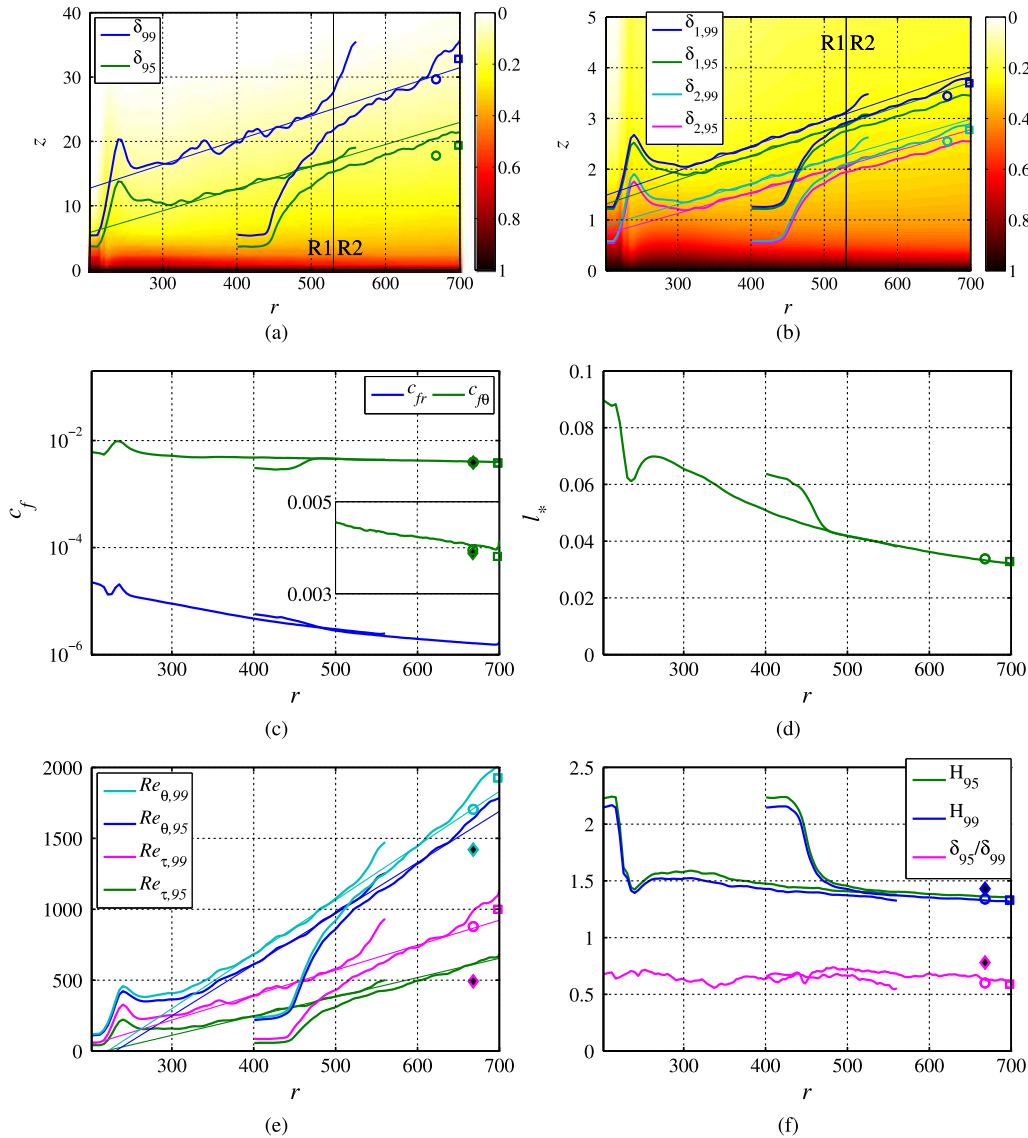
$$\delta_{1,95} = \int_0^{\delta_{95}} V_N \, dz, \quad \delta_{1,99} = \int_0^{\delta_{99}} V_N \, dz, \quad (8)$$

and the momentum-loss thicknesses as

$$\delta_{2,95} = \int_0^{\delta_{95}} V_N\left(1 - V_N\right) dz, \quad \delta_{2,99} = \int_0^{\delta_{99}} V_N\left(1 - V_N\right) dz. \quad (9)$$

The corresponding shape factors are $H_{95} = \delta_{1,95}/\delta_{2,95}$ and $H_{99} = \delta_{1,99}/\delta_{2,99}$, respectively. The friction Reynolds number can further

Fig. 3. Boundary-layer statistics averaged over $T = 1.625 - 4.625$ for case R1, and $T = 1.125 - 4.125$ for case R2. Rotating-disk experiments T01 and T02 from [10] are shown as $\bigcirc$ and $\square$, respectively, and the 2DTBL simulation 2D01 from [12] is shown as a black-filled diamond.

be defined as $Re_{\tau,95} = v_\tau \delta_{95} r$ (or $Re_{\tau,99} = v_\tau \delta_{99} r$), and the Reynolds number based on the momentum thickness as $Re_{\theta,95} = \delta_{2,95} r$ (or $Re_{\theta,99} = \delta_{2,99} r$).

The statistical quantities were azimuthally and temporally averaged, the time averaging starting at $T = 1.625$ and $T = 1.125$ for case R1 and R2, respectively. In Fig. 3 the resulting boundary-layer properties are shown from such an average: (a) boundary-layer thickness (δ_{95} and δ_{99}) on top of V_N; (b) displacement and momentum thickness ($\delta_{1,95}$, $\delta_{1,99}$, $\delta_{2,95}$ and $\delta_{2,99}$) on top of V_N; (c) skin-friction coefficients ($c_{fr} = 2(u_\tau/V_w)^2$ and $c_{f\theta} = 2(v_\tau/V_w)^2$); (d) the non-dimensional viscous length scale ($\ell_* = r^{-1}\sqrt{2/c_{f\theta}}$); (e) Reynolds numbers ($Re_{\tau,95}$, $Re_{\tau,95}$, $Re_{\theta,95}$, $Re_{\theta,99}$); and (f) shape factors (H_{95}, H_{99}) and δ_{95}/δ_{99}. In all figures the laminar boundary-layer properties are seen at the smallest r for both cases since the prescribed inflow is laminar.

The two simulations are shown simultaneously up to the radial edge position and experimental data from [10] are marked with a circle (T01, $\circ$) or a square (T02, $\square$). It should be noted that the comparison with the experiments may differ in absolute terms since the absolute values at a given r depend on the distance from,

and the strength of, the trip, and as can be seen in Fig. 3(a) there is a slight difference compared with the experimental data. At the end of the domain there may also be an edge effect that may affect the simulation data.

In Fig. 3(a), (b) and (e) linear curve fits to the boundary-layer thicknesses are shown for values between $r = 400$–500 from case R1. These curves are shown to agree with data from case R1 well beyond this radial range, and act as an extrapolation to case R2. In Fig. 3(b) it is clear that the values of case R2 are lower than those of case R1. These lower values correspond well to the experimental data compared to the linear extrapolation from case R1. For the inner region, (c) and (d) show that the properties from both simulations correspond well over a certain region. It is clear that case R2 has a region where the boundary layer is developing however around $r = 480$ both c_f and ℓ_* for case R2 have reached a similar level as those for case R1. Furthermore, in Fig. 3(e), the Re values of the two simulations seem to converge towards a linear increase with r, and follow the linear fit from case R1. This is, however, only at high r for case R2, before the edge effect takes place. In Fig. 3(f) the two simulations merge nicely
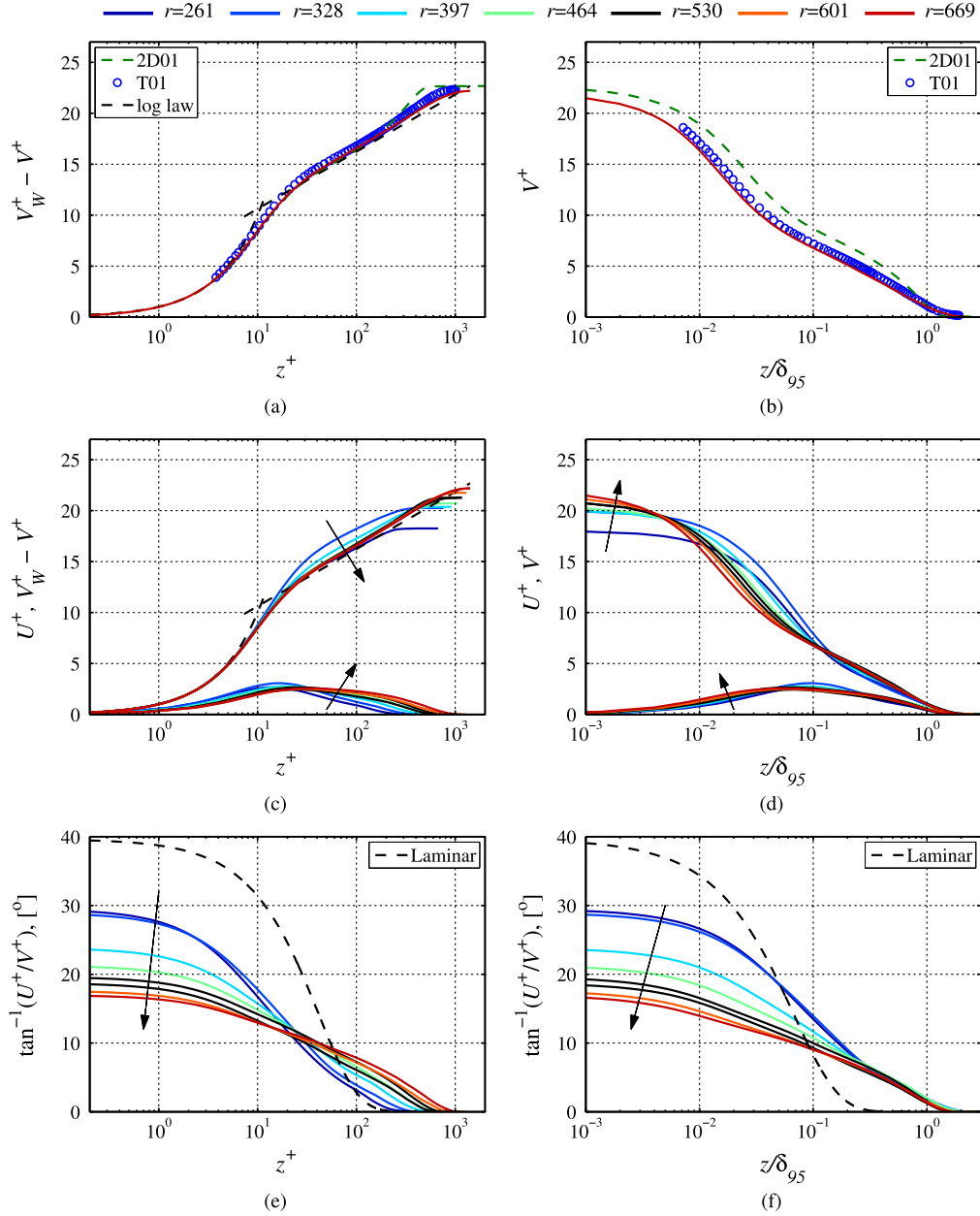
Fig. 4. Turbulent mean profiles. (a)–(b) Comparison between 2DTBL [12], experiments [10], and $r = 669$ for the present DNS. (c)–(d) Seven different r for the present DNS. (e)–(f) Mean flow angle as function of wall distance for all seven Reynolds numbers. The figures show inner (left column) and outer (right column) scalings, respectively. The logarithmic law seen as a dashed line in (a) and (c) has a Kármán constant $\kappa = 0.41$ and logarithmic intercept of 5.0.

around $r = 520$ and case R2 takes over for positions radially outwards. In the following figures both simulations are included where there is a change at radial position $r = 530$ from R1 to R2.

For the comparison to the 2DTBL, [12] (case 2D01), it is necessary to decide to which r the 2D-simulation should correspond. Imayama et al. [10] compared their experimental results to case 2D01 at $r = 668$ due to a similar skin-friction coefficient and we chose the same r for our comparison. As can be seen, the skin-friction coefficient, shown by a black-filled diamond in Fig. 3(c), is similar to T01 and R2. Diamonds showing 2D01 data are also found in Fig. 3(e) and (f), where $Re_{\tau,99}$ and $Re_{\theta,99}$ are lower than both simulations and experiments, and H_{99} and δ_{95}/δ_{99} are higher. Only experimental case T01 is further considered since T02 is just at the edge of our case R2.

3.2. Mean flow statistics and turbulent fluctuations

In the following section we use data from both simulations. From R1 we plot data for $r = 261, 328, 397, 464, 530$ and for R2 data from $r = 530, 601, 669$. Therefore, there are two sets of data for $r = 530$, which is the highest r for R1 and the lowest r for R2; they have developed from different initial conditions and these should not be expected to be perfectly identical. For the mean velocity the quantity commonly shown is $1 - V_N$ since this velocity profile can be compared to that of a flat plate with zero velocity at the wall and 1 in the free stream.

In Fig. 4(a)–(f) the mean velocities (azimuthal and radial) as well as the local horizontal flow angle are shown using the inner and outer length scales, respectively (the latter using δ_{95} as the scaling factor). The inner scaling is based on the azimuthal friction velocity
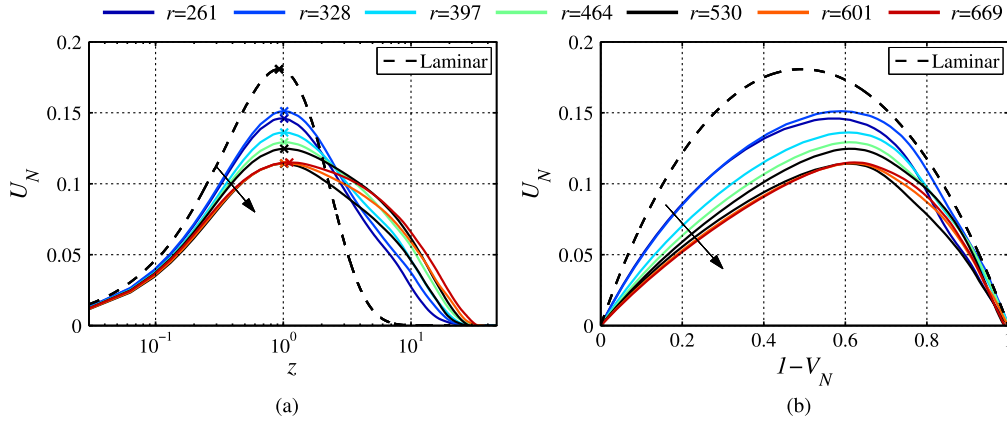
Fig. 5. $U_N = U/V_w$ plotted as function of (a) z and (b) $1 - V_N$. In (a) the symbol $\times$ marks the maximum.

(v_τ) for both the azimuthal and radial components. Also the viscous length scale ℓ_* is based on v_τ.[1]

In Fig. 4(a)–(b) the mean velocity profiles for $r = 669$ from the present case, the experiments and the 2DTBL can be compared. For the inner scaling (a), all three cases show a good correspondence, although the rotating-disk data do not show any obvious wake component, as also pointed out by [8]. For the outer scaling (b), there is now a significant difference between the 2DTBL and the rotating disk, because of the difference in the wake component.

In Fig. 4(c)–(d) both the azimuthal and radial mean velocities are plotted for seven Reynolds numbers, and as can be seen the maximum radial velocity is an order of magnitude smaller than the disk velocity. For $r = 669$, the value for the maximum of radial velocity as well as its position in the boundary layer are in good agreement with the results reported by [8], see their Fig. 3(b).

In Fig. 4(e)–(f) the local flow angle (in the $r\theta$-plane) is shown together with the flow angle for the laminar flow. As can be seen the flow angle decreases with Reynolds number and at the disk surface approaches a value close to 17°. This is larger than the flow angles reported in literature from experiments which are close to 11° [6,8,9], however is in good agreement with the LES results from [11] where the flow angle at the surface was found to be around 16°, for a slightly higher Re_θ of 2660.

The radial velocity component has a maximum that moves outwards in inner scaling (Fig. 4(c)) and inwards in outer scaling (Fig. 4(d)) when r increases. If instead U_N is plotted as function of z (see Fig. 5(a)), the maximum (marked by a cross) lies close to $z = 1$ for all r. This value is slightly larger than the position of the maximum for the laminar profile. In a polar plot (see Fig. 5(b)) similar to the one shown in Ref. [8] (their Fig. 4) it is clear why their estimate of the maximum skew angle of 11° is too small, this value was based on measurements for $1 - V_N \gtrsim 0.4$ whereas the largest angle occurs at the surface of the disk, i.e. $1 - V_N = 0$.

3.3. Reynolds stresses and turbulent kinetic energy budget

In Fig. 6(a)–(f) the fluctuating data of the azimuthal and radial velocities are shown. Fig. 6(a)–(c) show the azimuthal velocity fluctuations for a comparison between the same three cases as in Fig. 4(a)–(b), but here plotted scaled with (a) the friction velocity, (b) the wall velocity and in (c) as a local intensity. Overall the agreement is good however the experimental data show a lower value, especially close to the wall. This may be due to insufficient

spatial resolution of the hot-wire probe in the experiments. The maximum is located at $z^+ = 15$ with a value of $v_{rms}^+ = 2.7$, which is slightly lower than case 2D01. For the outer region, the disk simulations show slightly larger v_{rms} levels than both 2D01 and T01. In Fig. 6(d) the local intensity for all seven r is shown and increases with r, approaching a value of 0.4 in the near-wall region, corresponding well to the value obtained by [18]. In Fig. 6(e) and (f) u_{rms} and v_{rms} distributions are shown for both inner and outer scaling for all seven r.

It is also of interest to examine higher-order moments and here the skewness is presented, defined as

$$S_v = -\frac{\overline{v'^3}}{v_{rms}^3} \tag{10}$$

where overbar denotes a temporal and spatial average. Here, the skewness factor is defined with a negative sign in order to be comparable with the 2DTBL since in that case the high velocity is the free stream. There is a clear correspondence between cases 2D01, T01 and $r = 669$ from case R2 for the inner region shown in 7(a). In (b) there are some deviations in the outer region. Fig. 7(c) shows that the skewness is constant with r in the inner region in contrast to (d) showing the outer region. The deviation of $r = 261$ is due to the boundary layer not being fully developed at this position.

The turbulent kinetic energy (TKE) for the fluctuations is denoted by

$$k = \frac{\overline{u'u'} + \overline{v'v'} + \overline{w'w'}}{2}$$

and is shown in Fig. 8(a) together with its components, all normalized by v_τ^2. In (b) the Reynolds shear stresses are shown. By following the tensor notation the turbulent kinetic energy can be written $k = \overline{u_i'u_i'}/2$, and the full equation in Cartesian coordinates reads

$$\underbrace{\frac{\partial k}{\partial t} + U_j \frac{\partial k}{\partial x_j}}_{\text{convection}}$$

$$= \underbrace{-\overline{u_i'u_j'}\frac{\partial U_i}{\partial x_j}}_{\text{turbulent production}} \underbrace{-\frac{\partial}{\partial x_j}\left(\frac{1}{2}\overline{u_i'u_i'u_j'} + \frac{1}{\rho}\overline{u_j'p'} - \nu\frac{\partial k}{\partial x_j}\right)}_{\text{redistribution terms}} \tag{11}$$

$$\underbrace{-\nu\overline{\frac{\partial u_i'\partial u_i'}{\partial x_j\partial x_j}}}_{\text{viscous dissipation}}.$$

[1] If the total wall shear stress ($\tau_{w,tot} = \sqrt{\tau_{w,r}^2 + \tau_{w,\theta}^2}$) had been used to define the friction velocity it would have increased by a mere 2%.
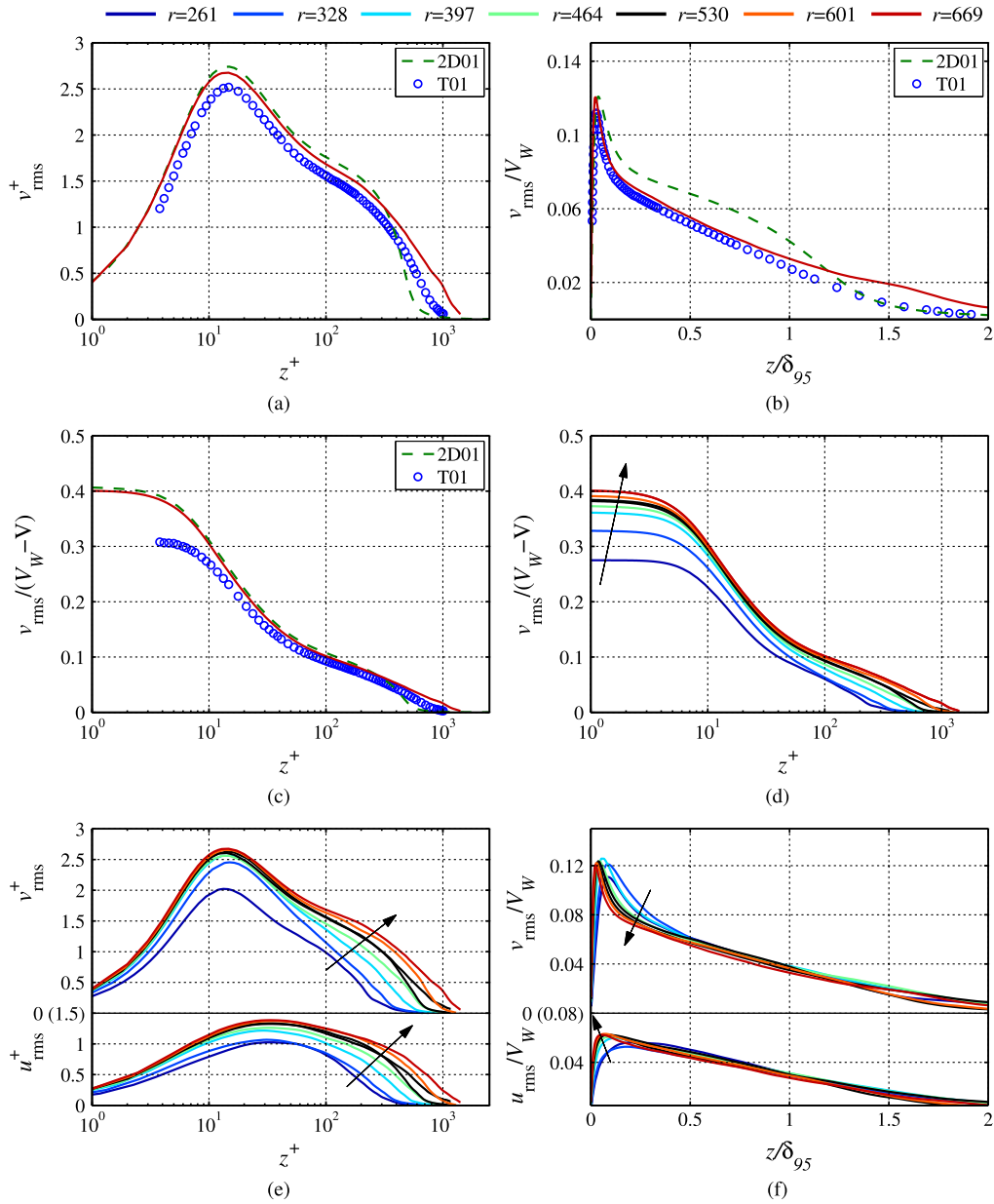
Fig. 6. Turbulent rms profiles. (a)–(c) Azimuthal rms plotted as a function of inner scaled wall distance, outer scaled wall distance, and local turbulence intensity against inner scaled wall distance. (d)–(f) All seven Reynolds numbers, (d) local turbulence intensity, (e) u_{rms}^+ and v_{rms}^+ as a function of z^+, (f) u_{rms}/V_w and v_{rms}/V_w as a function of z/δ_{95}.

Here, i and j are equal to x, y and z, and $U_z = W$ and $u_z' = w'$. Calculating each full term in Cartesian coordinates give scalars that do not have to be transformed to the cylindrical system. The turbulent production term is a measure of mean flow energy transfer to the turbulent fluctuations and is denoted by P^k. The spatial redistribution consists of three terms: the net effect of turbulent diffusion of $u_i'u_i'/2$ by u_j' (T^k); turbulent redistribution caused by the fluctuating pressure (Π^k); and the viscous diffusion of k (D^k). The viscous dissipation of the turbulent kinetic energy is further denoted by ε. The resulting data are shown in Fig. 9 for various Reynolds numbers including all terms. Commonly for boundary layers the viscous diffusion of k and the viscous dissipation balance each other close to the wall [19], which is also seen here. The peak in production is found around $z^+ = 12$ close to where v_{rms}^+ has a

maximum as expected, and also the terms T^k and Π^k are similar to those for a 2D turbulent boundary layer.

Finally we calculate the Townsend structure parameter A_1 which is defined as

$$A_1 = \frac{\left[(\overline{vw})^2 + (\overline{uw})^2\right]^{1/2}}{2k}$$

and gives a measure of the influence of the three-dimensionality of the flow. This is discussed at length by Littell and Eaton [8] since one of the motives of their study was to use the rotating disk TBL as an example of a three-dimensional TBL. However, as already mentioned they could not measure closer to the wall than approximately 100 viscous units. In Fig. 10 we show our DNS results together with the 2DTBL. This shows the difference between the three Reynolds numbers of the rotating-disk TBL and
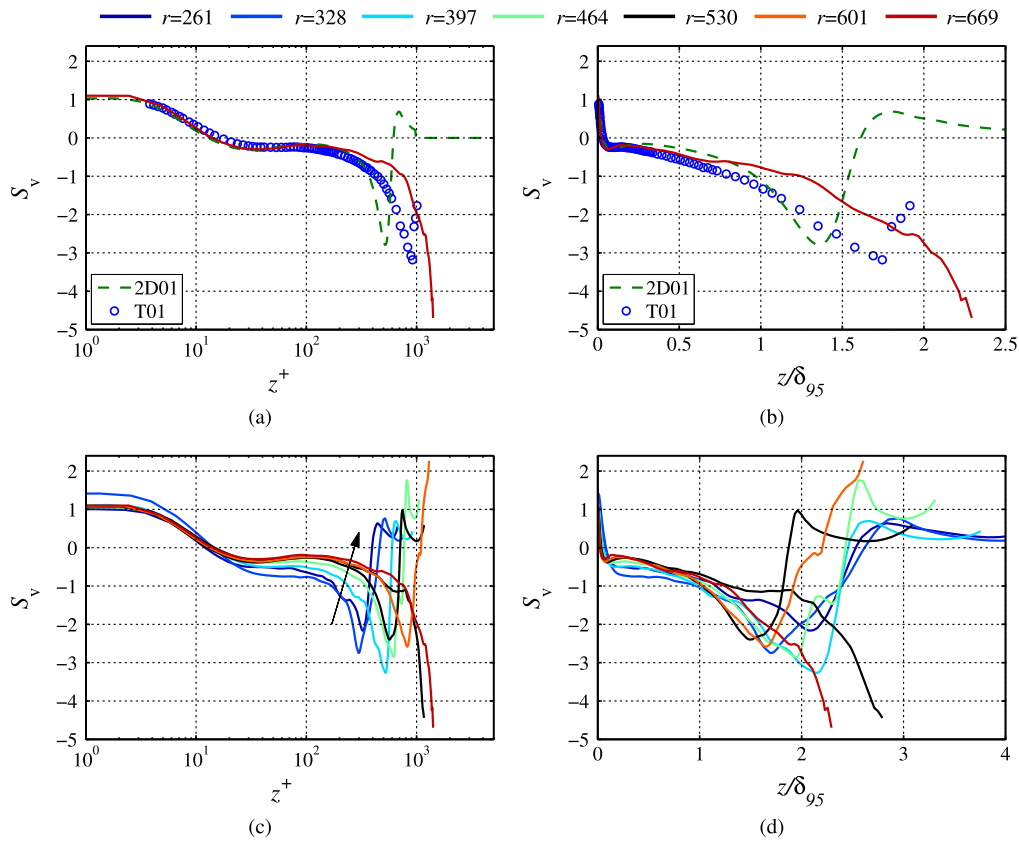
Fig. 7. Skewness of the azimuthal velocity fluctuations. (a)–(b) Comparison between present simulation, experiments by Imayama and 2DTBL, in inner and outer scaling, respectively. (c)–(d) Comparison between seven different simulation Reynolds numbers in inner and outer scaling, respectively.
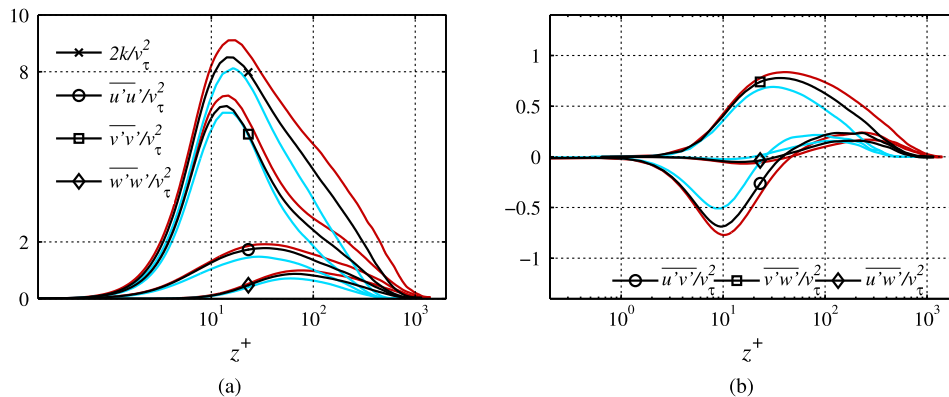
Fig. 8. (a) Twice the turbulent kinetic energy k and the corresponding values for the three different components, (b) the three Reynolds shear stresses. All terms are normalized by v_τ^2. $r = 397$ (blue), $r = 530$ (black, case R1) and $r = 669$ (red). (For interpretation of the references to colour in this figure legend, the reader is referred to the web version of this article.)

the 2DTBL is small, and, therefore, that the influence of the three-dimensionality on the turbulence is small.

3.4. Instantaneous velocity fields

In Figs. 11 and 12 instantaneous flow fields are shown for cases R1 and R2, respectively in the rotating reference frame. The colour scale gives the azimuthal velocity component (V_N), which is zero at the wall and hence near-wall fluid shows up in a reddish colour. Subfigure (a) in both cases show the $r\theta$-plane at $z = 0.4$ as well as a zR-plane. The turbulent region extends to about $r = 550$ and 700, respectively for the two cases. Since the viscous length scale decreases with r (see Eq. (6)), the distance from the wall

also changes along the radius and is approximately 7 and 11 for the two cases (for the ranges see the figure captions), hence in both cases the flow field shown is outside the viscous sublayer and in the buffer region. What is apparent in both cases are the long streaks of low-velocity fluid with patches of high velocity scattered in between. The Rz-plane shows large scales that give the boundary layer a ragged edge. In figures (b) and (c) parts of the $R\theta$-plane are expanded and shown for $z = 0.2$ and 0.4, respectively. They are taken at the same time instant and one can clearly see structures that are present at both levels.

From radial correlations of the azimuthal velocity fields (not shown here) one finds a zero-crossing of the correlation function followed by a minimum at $\Delta r = 2.6$ and 2.3 for cases R1 and R2
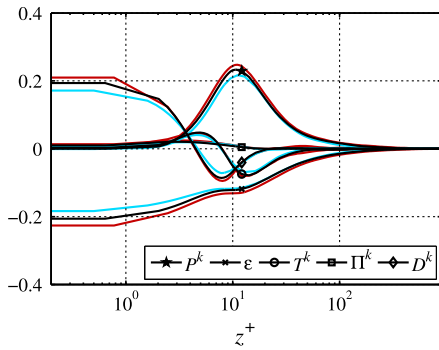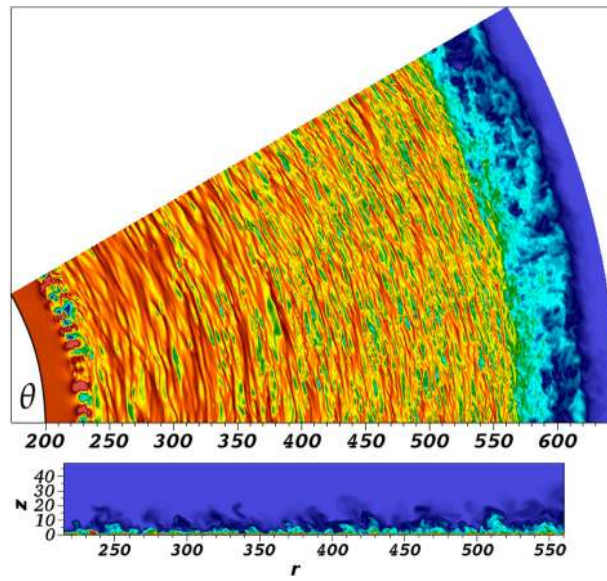
Fig. 9. All terms in Eq. (11). Showing $r = 397$ (blue), $r = 530$ (black, case R1) and $r = 669$ (red). (For interpretation of the references to colour in this figure legend, the reader is referred to the web version of this article.)
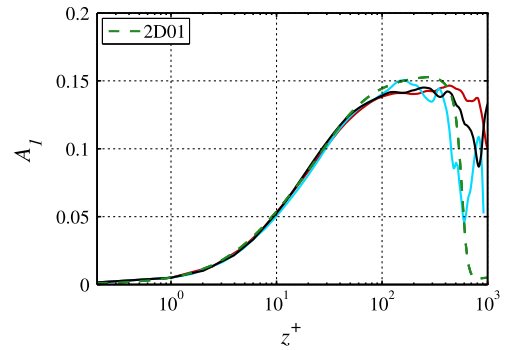
Fig. 10. The Townsend structure function $A1$ for three Reynolds numbers: $r = 397$ (blue), $r = 530$ (black, case R1) and $r = 669$ (red). Also shown are the data from the 2DTBL (2D01) as a dashed line. (For interpretation of the references to colour in this figure legend, the reader is referred to the web version of this article.)

(evaluated at $r = 400$ and $r = 600$ respectively) corresponding to about 50 and 65 in viscous units. If the minimum is interpreted as half the radial distanc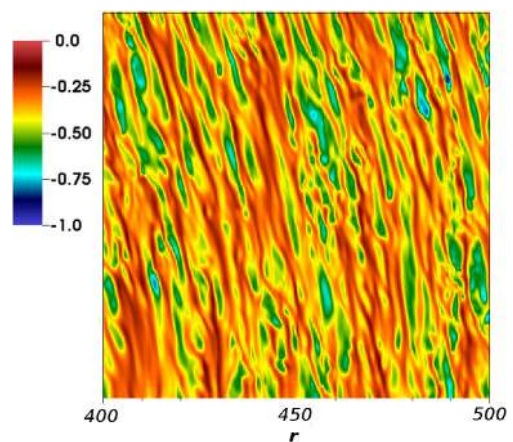e between the streaky structures, the distance between streaks is in the range of the spanwise scale of low-speed streaks observed for a 2DTBL which is usually given as approximately 100 (see for instance Ref. [20]).
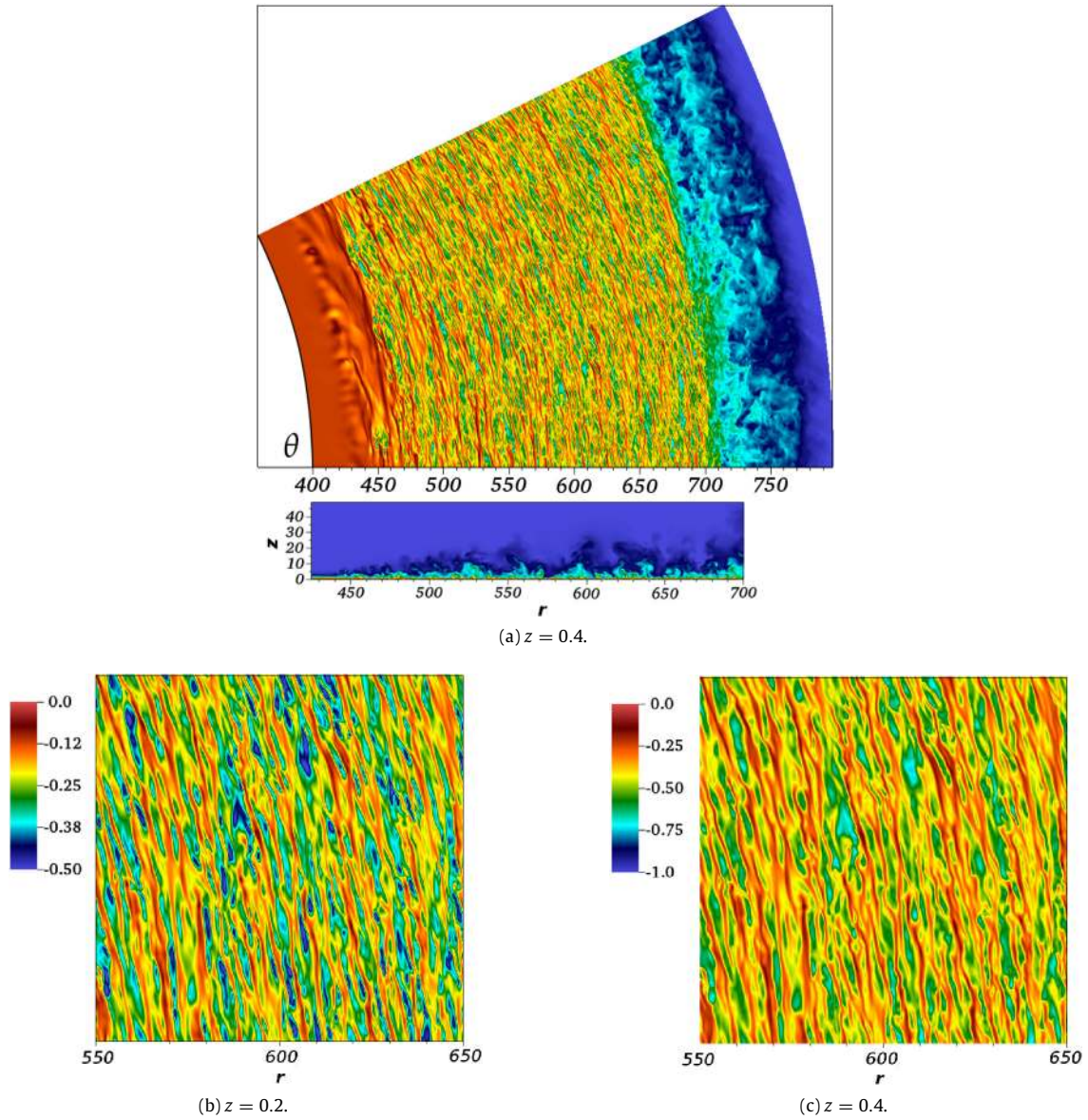

(a) $z = 0.4$.
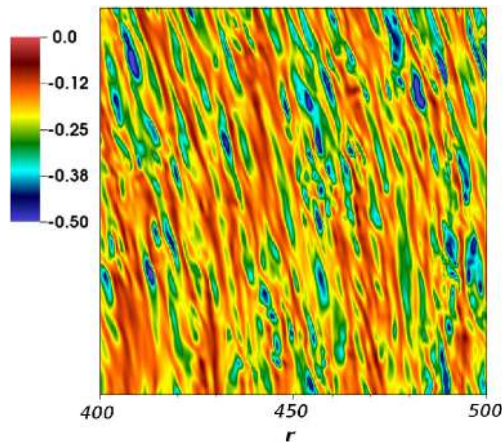
(b) $z = 0.2$.

(c) $z = 0.4$.

Fig. 11. Case R1 at $T = 2.25$ in the rotating reference frame. (b) and (c) show sections of (a) in greater detail. The same colour bar applies to (a) and (c). In (a) z^+ ranges from 5.8 ($r = 280$) to 10.3 ($r = 550$), in (b) $z^+ = 4.4$ at $r = 450$ and in (c) $z^+ = 8.7$ at $r = 450$. (For interpretation of the references to colour in this figure legend, the reader is referred to the web version of this article.)

(a) $z = 0.4$.

(b) $z = 0.2$.   (c) $z = 0.4$.

Fig. 12. Case R2 at $T = 1.75$ in the rotating reference frame. (b) and (c) show sections of (a) in greater detail. The same colour bar applies to (a) and (c). In (a) z^+ ranges from 9.5 ($r = 500$) to 12.4 ($r = 700$), in (b) $z^+ = 5.5$ at $r = 600$ and in (c) $z^+ = 11.0$ at $r = 600$. (For interpretation of the references to colour in this figure legend, the reader is referred to the web version of this article.)

(a)   (b)
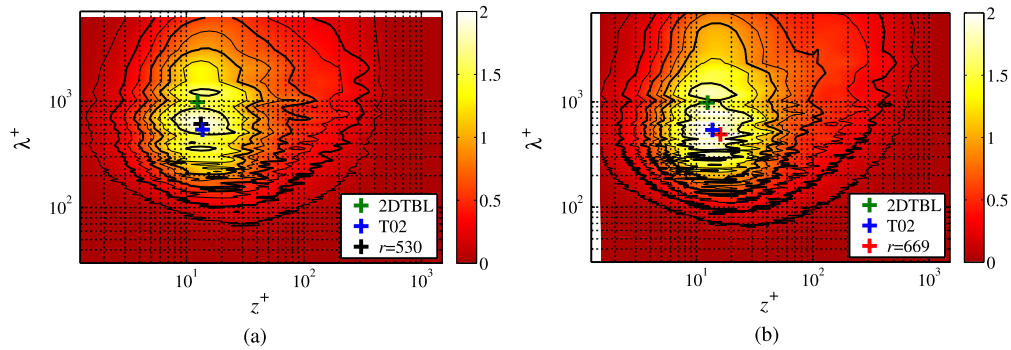
Fig. 13. Premultiplied ($\lambda^+ E^+$) spectral maps. The black contours correspond to [0.1 **0.25**, 0.4, **0.575**, 0.775, **0.95**, 1.2, **1.6**]. Bold numbers correspond to thicker contour lines. (a) $r = 530$, (b) $r = 669$.

3.5. Spectral maps

Spectral maps of the azimuthal velocity fluctuations for case R2 at $r = 530$ and 669 are shown in Fig. 13. They were obtained by a Fourier analysis in the azimuthal direction using 216 instantaneous fields giving the spectral density E. The data are presented in premultiplied form, i.e. E is multiplied with λ, where λ is the wavelength in the azimuthal direction. The maxima of the spectra are shown by markers, and additional markers are shown from experiment T02 at $R = 698$ [10] and the simulation data from [12] for the 2DTBL for $Re_\tau = 2500$, i.e. different data than previously shown. The Reynolds numbers are not fully comparable, although both figures show that the maxima of the rotating-disk boundary layer are obtained for shorter wavelengths than the 2DTBL, which may be an influence of the streak angle with respect to the azimuthal direction.

4. Summary

Direct numerical simulation data of the turbulent boundary layer on a rotating disk have been extensively compared to previous rotating-disk experiments [10] and data from a flat-plate turbulent boundary layer (2DTBL) [12]. Also other previous experiments and one LES study of the rotating-disk turbulent boundary layer have been used for comparison. The simulations presented correspond well to experiments for the azimuthal mean flow and turbulent statistics [10]. Compared to the 2DTBL, a missing wake region and a lower shape factor are shown for the rotating disk, in agreement with previous results. The missing wake region is also found for the asymptotic suction turbulent boundary layer (see Refs. [21,22]) and may be a result of that the outer flow, both for the rotating disk and the suction boundary layer, is moving towards the surface, in contrast to the 2DTBL.

The v_{rms} level in the near-wall region is, however, shown here to be of similar amplitude to the 2DTBL, in contrast to earlier experimental measurements by [10]. The v_{rms}^+ peak is in agreement for all cases located around $z^+ = 15$. Furthermore, the simulations provide data showing the development of the statistics with Reynolds number, for example showing a peak in the mean radial velocity located at $z = 1$ for all radial positions. The local flow angle (skew angle) is largest at the surface of the disk and decreases with Reynolds number, but seems to approach a value around 17°, which is higher than previously reported. Despite the rather strong crossflow component the Townsend structural parameter, A_1, is almost indistinguishable from that of the 2DTBL, in contrast to the results reported by [8]. All Reynolds stresses, the kinetic energy budget terms are also provided along with the spectral maps and these compare well with the 2DTBL however shorter azimuthal wavelengths are found in the near-wall region, in agreement with the results of [10].

Acknowledgements

Appendix

A.1. Calculations of higher order terms

The velocity can be divided into a mean and a fluctuating part: $u_i = U_i + u_i'$. In the simulation we collect mean values of the first four moments, i.e. u_i, u_i^2, u_i^3 and u_i^4. From these it is possible to obtain the mean value and the first three central moments of u_i' such that:

$$U_i = \overline{u_i} \tag{A.1}$$

$$\overline{u_i'^2} = \overline{u_i^2} - U_i^2 \tag{A.2}$$

$$\overline{u_i'^3} = \overline{u_i^3} - 3\overline{u_i'^2}U_i - U_i^3 = \overline{u_i^3} - 3\overline{u_i^2}U_i + 2U_i^3 \tag{A.3}$$

$$\begin{aligned}\overline{u_i'^4} &= \overline{u_i^4} - 4\overline{u_i'^3}U_i - 6\overline{u_i'^2}U_i^2 - U_i^4 \\ &= \overline{u_i^4} - 4\overline{u_i^3}U_i + 6\overline{u_i^2}U_i^2 - 3U_i^4.\end{aligned} \tag{A.4}$$

Similarly it is possible to get the Reynolds shear stress terms as $\overline{u_i'u_j'} = \overline{u_iu_j} - U_iU_j$ if the mean values of u_iu_j are calculated during the simulation. Similarly higher order products needed to obtain other physical quantities can also be calculated. However all these terms are expressed in the Cartesian coordinate system and need to be transformed to the (r, θ, z)-system. For details of this transformation see Appendix A.2.

The equation for the kinetic energy of the turbulent velocity fluctuations is given by Eq. (11). Also all the correlation terms $\overline{u_i'u_i'u_j'}$ and $\overline{u_j'p'}$ can be calculated by averaging $u_iu_iu_j$ and u_jp during the simulation. The derivatives needed to, for example, the dissipation term, are done directly in the code with spectral accuracy. The full terms of the kinetic energy equation are scalars and therefore no transformation between the two coordinate systems is necessary.

A.2. Coordinate transformations

The conversion between the Cartesian coordinates used in the simulation code and the cylindrical coordinates for the physical analysis of the flow field is done using a transformation matrix

$$\mathbf{Q} = \begin{bmatrix} \cos\theta & \sin\theta & 0 \\ -\sin\theta & \cos\theta & 0 \\ 0 & 0 & 1 \end{bmatrix}. \tag{A.5}$$

This transformation can be applied to various orders of tensors. Transforming the velocity vector from the Cartesian coordinates the first order transformation $\mathbf{U} = \mathbf{Q}\mathbf{U_x}$ is used. Further transforming a second order tensor, e.g. Reynolds stress terms, the second order transformation $\mathbf{U}\mathbf{U}^T = \mathbf{Q}\mathbf{U_x}\mathbf{U_x}^T\mathbf{Q}^T$ is used, commonly known as 'the Mohr transformation'. The transformations up to fourth order using tensor notation can be written as

$$U_i = Q_{i,j}U_{x|j}$$
$$U_{i,j} = Q_{i,p}Q_{j,q}U_{x|p,q}$$
$$U_{i,j,k} = Q_{i,p}Q_{j,q}Q_{k,r}U_{x|p,q,r} \tag{A.6}$$
$$U_{i,j,k,l} = Q_{i,p}Q_{j,q}Q_{k,r}Q_{l,s}U_{x|p,q,r,s}$$

where the matrices are expanded from one row to the next.

References

[1] T. von Kármán, Über laminare und turbulente Reibung, Z. Angew. Math. Mech. 1 (1921) 232–252.

[2] E. Appelquist, P. Schlatter, P.H. Alfredsson, R.J. Lingwood, On the global non-linear instability of the rotating-disk flow over a finite domain, J. Fluid Mech. 803 (2016) 332–355.

[3] S. Imayama, P.H. Alfredsson, R.J. Lingwood, An experimental study of edge effects on rotating-disk transition, J. Fluid Mech. 716 (2013) 638–657.

[4] E. Appelquist, P. Schlatter, P.H. Alfredsson, R.J. Lingwood, Transition through convective instability in the rotating-disk boundary-layer flow, J. Fluid Mech. 836 (2018) 43–71.

[5] R.J. Lingwood, P.H. Alfredsson, Instabilities of the von Kármán boundary layer, Appl. Mech. Rev. 67 (2015) 030803.

[6] T.-S. Cham, M.R. Head, Turbulent boundary-layer flow on a rotating disk, J. Fluid Mech. 37 (1969) 129–147.

[7] F.F. Erian, Y.H. Tong, Turbulent flow due to a rotating disk, Phys. Fluids 14 (1971) 2588–2591.

[8] H.S. Littell, J.K. Eaton, Turbulence characteristics of the boundary layer on a rotating disk, J. Fluid Mech. 266 (1994) 175–207.

[9] M. Itoh, I. Hasegawa, Turbulent boundary layer on a rotating disk in infinite quiescent fluid, JSME Int. J. 37 (1994) 449–456.

[10] S. Imayama, R.J. Lingwood, P.H. Alfredsson, The turbulent rotating-disk boundary layer, Eur. J. Mech. B Fluids 48 (2014) 245–253.

[11] X. Wu, K.D. Squires, Prediction and investigation of the turbulent flow over a rotating disk, J. Fluid Mech. 418 (2000) 231–264.

[12] P. Schlatter, R. Örlü, Assessment of direct numerical simulation data of turbulent boundary layers, J. Fluid Mech. 659 (2010) 116–126.

[13] P.F. Fischer, J.W. Lottes, S.G. Kerkemeier, Nek5000, 2012. Web page. http://nek5000.mcs.anl.gov.

[14] A.T. Patera, Aspectral element method for fluid dynamics: Laminar flow in a channel expansion, J. Comput. Phys. 54 (1984) 468–488.

[15] Y. Maday, A.T. Patera, Spectral element methods for the incompressible Navier–Stokes equations, in: A.K. Noor, J.T. Oden (Eds.), State-of-the-Art Surveys on Computational Mechanics, ASME, 1989, pp. 71–143.

[16] G.E. Karniadakis, M. Israeli, S.A. Orszag, High-order splitting methods for the incompressible Navier–Stokes equations, J. Comput. Phys. 97 (1991) 414–443.

[17] P. Schlatter, R. Örlü, Turbulent boundary layers at moderate Reynolds numbers: inflow length and tripping effects, J. Fluid Mech. 710 (2012) 5–34.

[18] P.H. Alfredsson, A.V. Johansson, J.H. Haritonidis, H. Eckelmann, On the fluctuating wall shear stress and velocity field in the viscous sublayer, Phys. Fluids 31 (1988) 1026–1033.

[19] S.B. Pope, Turbulent Flows, Cambridge University Press, ISBN: 978-0-5215-9886-6, 2000.

[20] S. Kline, W. Reynolds, F. Schraub, P. Rundstadler, The structure of turbulent boundary layers, J. Fluid Mech. 30 (1967) 741–773.

[21] S. Yoshioka, P.H. Alfredsson, Control of turbulent boundary layers by uniform suction and blowing, in: R. Govindarajan (Ed.), IUTAM Symposium on Laminar–Turbulent Transition, Fluid Mechanics and Its Applications, Vol. 78, Springer, 2006, pp. 437–442.

[22] A. Bobke, R. Örlü, P. Schlatter, Simulations of turbulent asymptotic suction boundary layers, J. Turb. 17 (2016) 157–180.